JGR Oceans

Key Points:

- Subsurface tropical instability waves (subTIWs) are identified in simulations and observations in the tropical Atlantic Ocean for the first time
- SubTIWs are generated by baroclinic and barotropic conversion both north and south of the Equator
- Despite similar characteristics, surface and subsurface TIWs are distinct waves which both impact thermocline dynamics

Identifying and Characterizing Subsurface Tropical Instability Waves in the Atlantic Ocean in Simulations and Observations

Mia Sophie Specht[1,2] [iD], **Johann Jungclaus[1]** [iD], **and Jürgen Bader[1]** [iD]

[1]Max Planck Institute for Meteorology, Hamburg, Germany, [2]Max Planck Institute for Meteorology, International Max Planck Research School of Earth System Modelling, IMPRS, Hamburg, Germany

Abstract Recent observations in the Pacific Ocean suggest that, apart from tropical instability waves (TIWs) at the surface, there also exist subsurface tropical instability waves (subTIWs), which can alter vertical mixing. However, the extent to which subTIWs impact mixing and heat flux is still unknown. Moreover, studies on subTIWs have been conducted exclusively in the Pacific. Here, we show the presence of subTIWs in the Atlantic for the first time, using mooring observations. Analyzing 16 years of simulations of a comprehensive, global, high-resolution ocean model, we characterize subTIWs in the Atlantic with regard to their spatial and temporal variability and investigate their influence on vertical mixing. We find subTIWs in the Atlantic between 40 and 90 m depth in both the model and observations. Furthermore, the model results reveal that unlike TIWs, subTIWs frequently also occur south of the Equator in the Atlantic Ocean. We show that subTIWs induce an oscillating multilayer shear structure, suggesting subTIWs to destabilize the mean flow and thereby induce mixing. This is strongest north of the Equator, where both TIWs and subTIWs act simultaneously. We conclude that despite similar characteristics, TIWs and subTIWs are distinct waves which both impact mixing and heat flux within the thermocline. Therefore, future studies of thermocline dynamics in the tropical oceans should not only consider TIWs but also take into account the effect of subTIWs, particularly in the subTIW dominated region south of the Equator.

Plain Language Summary Tropical instability waves (TIWs) cause sharp changes in ocean surface temperature. This influences the atmosphere above, and by extension, affects weather and climate over the tropical oceans and nearby countries. TIWs can also affect downward mixing of, for example, temperature and CO_2 from the surface, which is important for the climate system. Observations in the Pacific Ocean show the existence of similar waves in the subsurface, called subsurface TIWs (subTIWs), which can alter the effects of TIWs. Here, we show for the first time that subTIWs also exist in the Atlantic Ocean. We characterize their spatial pattern and their influence on vertical mixing, using output from the high-resolution ocean model ICON-O. In both observations and model output, we find subTIWs in the Atlantic Ocean between 40 and 90 m depth. Unlike TIWs, subTIWs are active in both hemispheres. We also show that subTIWs can destabilize subsurface ocean currents and thereby change mixing. This is strongest north of the Equator, where TIWs and subTIWs act simultaneously. We conclude that subTIWs are an important feature of the Atlantic Ocean, and suggest that future assessments of upper ocean dynamics should not be limited to the effect of TIWs alone but also include subTIWs.

1. Introduction

Temperature and velocity variability in the Tropical Atlantic Ocean are dominated by the seasonal cycle and interannual to decadal variability, such as the Atlantic meridional and zonal mode (Busalacchi & Picaut, 1983; Cabos et al., 2019; Carton et al., 1996; Deppenmeier et al., 2016; Lübbecke et al., 2018; Muñoz et al., 2012; Murtugudde et al., 2001; Prodhomme et al., 2019; Tourre et al., 1999; Xie & Carton, 2004). However, the dominant feature of intraseasonal variability, tropical instability waves (TIWs) have been found to be significant for the mixed layer heat budget and air-sea interactions in the tropical Atlantic (Bunge et al., 2007; Grodsky et al., 2005; Jochum & Murtugudde, 2006). A recent study by Liu et al. (2019) states that TIWs can have complex vertical velocity structures, which interact with the zonal mean flow and thereby impact vertical mixing. In the equatorial Pacific Ocean this is true particularly for the oscillating zonal

component of TIWs. Despite large efforts to understand the horizontal structure and generation mechanisms of surface-intensified TIWs, such vertical structures of TIWs and their impact on vertical mixing have been scarcely studied. In a novel approach to study the vertical structure of TIWs, Liu et al. (2019) used observed temperature and velocity records from a mooring at 0°N, 140°W to show the existence of subsurface mode tropical instability waves (subTIWs) in the tropical Pacific. The vertical shear caused by such subTIWs can interact nonlinearly with the shear of the zonal mean flow and largely change the total shear above the Equatorial Undercurrent (EUC) core, suggesting that subTIWs play an important role in vertical heat transport and mixing (Liu et al., 2019, 2020). Furthermore, subTIWs may alter the character of TIWs. However, these results are based on a single spot mooring in the equatorial Pacific and therefore, neither horizontal structure nor generation mechanisms of subTIWs have been determined (Liu et al., 2019). Hence, while TIWs are an extensively studied feature of all tropical oceans, to date little is known about subTIWs and the existence of subTIWs in the Atlantic is yet to be shown.

In this study, we show the existence of subTIWs in the Atlantic for the first time, using observations from two moorings at 4°N, 23°W and 0°N, 23°W and 16 years (2003–2019) of daily temperature and velocity output from the global, comprehensive, high resolution (10 km) setup of the ocean model ICON-O (ICOsahedral Non-hydrostatic-Ocean). Spatio-temporal analyses of subTIWs require using model simulations because observations are too sparse, in both spatial and temporal domain. The continuous simulation over almost two decades allows for statistically more robust analyses compared to the few years of available observations. In particular, subTIW year-to-year variability and the relevance of subTIW-induced variability relative to variability on longer time scales, such as the seasonal cycle, can be assessed. We take advantage of the horizontal and vertical high-resolution ICON-O model output to investigate the spatial distribution of subTIWs and their impact on vertical mixing in different regions of the tropical Atlantic. We assess the relative importance of subTIWs compared to TIWs for vertical mixing, and the role of subTIWs in altering vertical and horizontal heat fluxes. Furthermore, we analyze the combined effect of simultaneous occurrence of TIWs and subTIWs on vertical mixing and heat fluxes.

We find that subTIWs are present in the tropical Atlantic with characteristics distinctively different from the ones known for surface-intensified TIWs. In particular, unlike TIWs, subTIWs are most prominent away from the Equator in both northern and southern hemisphere. The main occurrence period of subTIWs is one to three months later than the occurrence of surface-intensified TIWs. In agreement with Liu et al. (2019), our results suggest that subTIWs can alter vertical mixing above the thermocline. Since subTIWs can occur at different times, in greater depth and in different regions than TIWs, the effect of subTIWs on mixing is not included when only studying TIWs. Furthermore, we show that the impact on vertical mixing and heat flux is largely increased by the simultaneous occurrence of TIWs and subTIWs. Hence, it is important to consider both TIWs and subTIWs when studying upper ocean dynamics in the tropical Atlantic, as well as studying TIW/subTIW interaction.

2. Data

2.1. Observational Data

2.1.1. Hourly Mooring Data at 4°N, 23°W

Observations at 4°N, 23°W used in this study are part of the Tropical Atlantic Current Observation Study (TACOS) which measures upper ocean velocity and shear at the 4°N, 23°W Prediction and Research Moored Array in the Tropical Atlantic (PIRATA) mooring (Bourlès et al., 2019; Perez et al., 2019). The TACOS mooring data were first analyzed and described in detail in Perez et al. (2019). It provides a unique high-resolution 1-year data set (March 6, 2017 to March 26, 2018) which allows for assessing the temporal and vertical current structure at this location (Perez et al., 2019).

In this study, we analyze data from 10 downward facing point acoustic current meters mounted on the mooring, with sample volumes centered at 7, 12, 17, 22, 27, 32, 37, 47, 57, 66.6, and 86.6 m (hereafter, the last two will be referred to as 67 and 87 m, respectively, as done by Perez et al., 2019). Details on the individual lengths of each sensor record and their mean values can be found in Perez et al. (2019). Data gaps occur at individual sensor depths, as shown in Figure 1a. Thus, we filled these gaps by interpolating over depth between the sensors directly above and below the errant sensor. Finally, we interpolated all mooring data
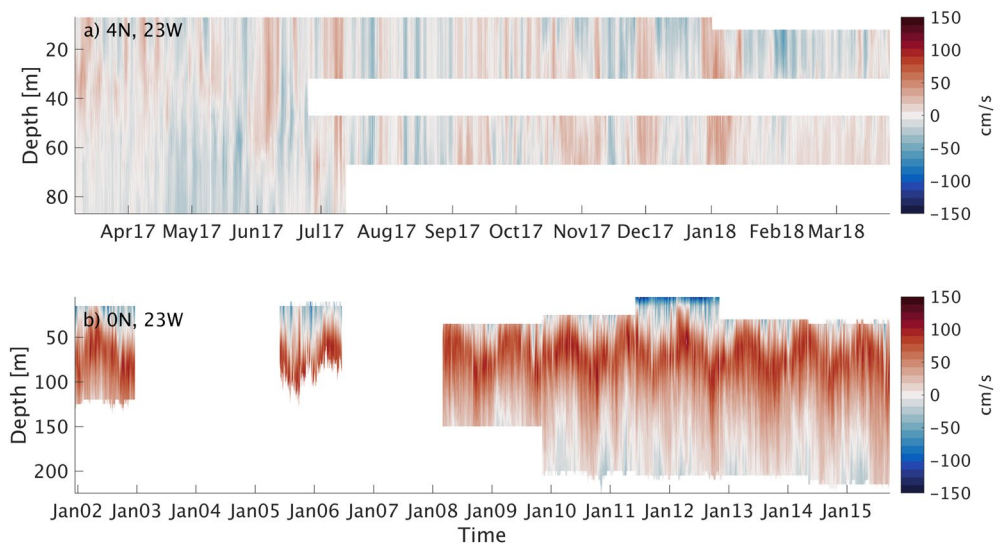
Figure 1. Available zonal velocity records at 4°N, 23°W (a) and 0°N, 23°W (b) since mooring deployment. Velocities are given in *cm/s*. Positive values indicate eastward velocities, negative values indicate westward velocities.

onto a regular 2 m depth grid for direct comparison with the model data and observations at 0°N, 23°W. We did not extrapolate the missing velocity data at 87 m after July 2017. Instead we focus our analysis on the upper 67 m.

2.1.2. Hourly Mooring Data at 0°N, 23°W

Hourly velocity records at 0°N, 23°W are available from an acoustic doppler current profiler (ADCP) mooring at the PIRATA mooring site. At this location, subsurface ADCPs were moored since 2001 (Bourlès et al., 2019). Available zonal velocity records are shown in Figure 1b. Unfortunately, large gaps exist in the velocity records, from December 2002 to June 2005 and from June 2006 to March 2008. Records before March 2008 are only available between 15 and 120 m. From March 2008 to September 2015, velocities were measured between 25 and 210 m. From June 2011 to November 2012, records are also available near the surface between 5 and 25 m (Figure 1b). Due to the sparsity of velocity data before 2008, we only use observations from 2008 onwards. Small temporal gaps are filled by linear interpolation. Furthermore, during periods where velocity records start below 30 m depth, we extrapolate vertically to gain a consistent data set between 30 and 120 m. This allows us to study both TIWs and subTIWs in a multiyear data set. Furthermore, similar to the observations at 4°N, 23°W, we interpolated the data onto a regular 2 m vertical grid for comparison.

2.2. ICON-O Model Setup

We examine the spatial extent of subTIWs and their regional effects on vertical mixing using a high-resolution setup of the global, comprehensive ocean component of the ICON model, ICON-O. ICON-O is part of the ICON framework which has a nonhydrostatic atmosphere (Giorgetta et al., 2018; Zängl et al., 2015). However, despite the name, the nonhydrostatic approach is not realized in the ocean component of the model framework. Instead, ICON-O has a hydrostatic ocean. Details on ICON-O, regarding the underlying icosahedral grid, model equations and the spatial and temporal discretization can be found in Korn (2017). The particular ICON-O setup used in this study has a horizontal resolution of 10 km and 128 vertical levels with a high number of layers in the upper ocean (12 layers in the upper 100 m, not equally spaced). Simulation of vertical mixing is based on a prognostic equation for turbulent kinetic energy (TKE) (Gaspar et al., 1990). The model has undergone a spin-up period of 25 years, during which it is forced by 24 hr Ocean Model Intercomparison Project (OMIP) data (Röske, 2006) starting from the Polar Science Center Hydrographic Climatology (PHC) (Steele et al., 2001). The spin-up is followed by a simulation period from 1948 to 1978, forced by 6 hr NCEP data (Kalnay et al., 1996). This part of the model setup is similar to the previous STORM simulations with ICON-O's predecessor MPI-OM as described in Storch et al. (2012). From January

1979 to December 2019, the ocean is forced by hourly ERA5 reanalysis data (Hersbach et al., 2020), which by the time of the model simulation was available from 1979 onwards. ERA5 provides hourly output at increased grid spacing of 31 km globally and 137 levels in the vertical level, compared to the 6-hourly output at 79 km on 60 vertical levels in ERA-Interim (Hersbach et al., 2019, 2020). For the analyses, only the output from the period February 2003 to December 2019 is considered. From the global model output of daily and monthly 3D velocity fields, temperature, and salinity, we select a region from 10°S to 10°N and 60°W to 20°E to study subTIWs in the Atlantic Ocean. Furthermore, prior to the analyses, we interpolate all model output from the original icosahedral grid onto a regular grid with 0.1° × 0.1° horizontal grid spacing using nearest neighbor interpolation.

3. Methods

3.1. Identifying SubTIWs

We identify subTIWs in the equatorial Atlantic in both model and observations, under consideration of the subTIW characteristics found in the equatorial Pacific by Liu et al. (2019). Following Liu et al. (2019), velocity anomalies in the TIW period band vary with depth and show distinct peaks in the subsurface layer. When applying a narrower temporal band-pass filter to isolate subTIWs from TIWs, they find oscillating zonal velocities clearly centered in the subsurface, which they suggest to be the manifestation of subTIWs. Unlike the study by Liu et al. (2019), our analysis is not solely based on mooring data. Hence, we first need to identify the regions in which instability waves are strongest in the Atlantic. Based on these regions, we then define the temporal band-pass filtering window for subTIWs in the tropical Atlantic. To identify subTIW dominated regions, similarly to the methods used by de Decco et al. (2018), we filter the model temperature output using a 2D Gaussian filter, which we first apply in time and then in space. The chosen band-pass filtering width allows oscillations with a period of 15–60 days and wavelengths of 4 to 20° longitude (≈400–2,000 km) to pass. These are the periods and wavelengths of TIWs in the Atlantic, which were found in previous studies (e.g., de Decco et al., 2018). It is reasonable to assume that subTIWs reside within the same period and wavelength window. We compute the standard deviation of the filtered temperature in a 4-month moving average window at each grid point in an area from 10°S to 10°N in the Atlantic, for the entire simulation period and each model layer within the thermocline. This approach for finding strong instability wave events is modified following the method applied in Perez et al. (2019). We combine the resulting time series of temperature standard deviation for each grid point to determine the 90th percentile of temperature standard deviation for the chosen model domain of 10°S to 10°N in the Atlantic. The resulting value for the domain wide 90th percentile, calculated for each model layer, is taken as the threshold value for strong instability wave activity. At each grid point, we count the total number of events above the calculated 90th percentile temperature threshold during the simulation period. As such, we construct a 2D histogram of strong instability wave events in all model layers in the thermocline. In the subsurface, instability waves are most pronounced in 64 m depths. Here, two regions of strong events can be found. One of them is located north of the Equator at 2.5 to 5°N, 12 to 22°W (hereafter called Region North), the other one is located south of the Equator at 1 to 3°S, 15 to 28°W (hereafter called Region South). Figure 2 shows the 2D histogram of strong instability wave events in 64 m depth and the chosen regions on which our analyses focus in the following. The locations of the two moorings used in this study are shown as dots. Furthermore, the dashed box in Figure 2 shows the region in which strong TIW activity at the surface can be found, called Region Equator (0 to 2°N, 9 to 19°W). This region is determined using 2D histograms of strong instability waves at the surface.

Next, we conduct wavelet and spectral analysis of the meridional and zonal velocity time series at 64 m depth to find the individual subTIW periods in each region. Both power spectral density and wavelet transforms are calculated for each grid point and averaged afterward to gain a box averaged power spectrum and wavelet transform. The averaged wavelet transforms are shown in Figures 4b and 4d and will be described in detail in Section 4.2. Figures 4a and 4c show all individual spectra (gray lines) as well as the resulting mean (black line) and the chosen filtering periods (red shading). Unlike Liu et al. (2019), we use both wavelet analysis and power spectral density analysis to identify subTIW periods to take into account varying periods in the different regions and years. This method results in an average subTIW period of 24–53 days in Region North and 25–47 days in Region South. For the observational data, resulting subTIW periods are
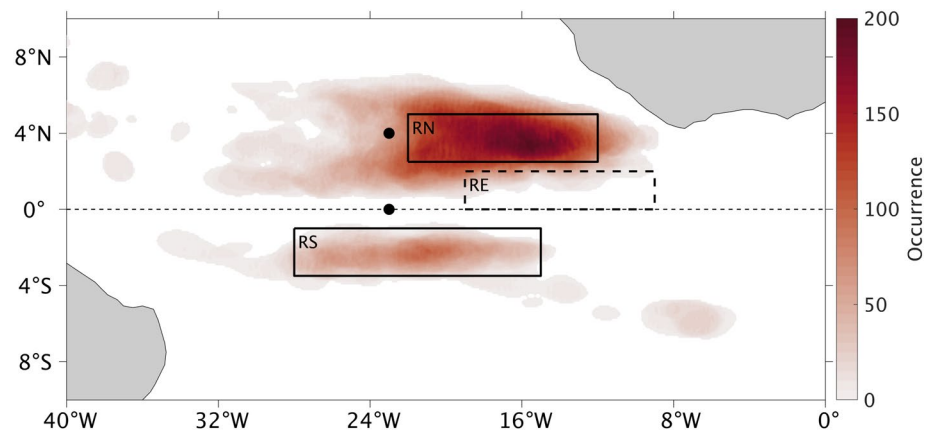
Figure 2. 2D histogram of strong subsurface tropical instability wave (subTIW) occurrence in 64 m depth in the study region during the entire 16- year simulation period. Black dots indicate the location of the Prediction and Research Moored Array in the Tropical Atlantic (PIRATA) mooring sites (0°N, 23°W and 4°N, 23°W), black solid boxes mark the identified subTIW regions. Region North (RN): 2.5 to 5°N, 12 to 22°W. Region South (RS): 1 to 3.5°S, 15 to 28°W. Black dashed box marks the region of pronounced TIW activity at the surface, Region Equator (RE): 0 to 2°N, 9 to 19°W.

26–30 days at 0°N, 23°W and 30–45 days at 4°N, 23°W. Hence, to study pure subTIW dynamics, we apply a 2D Gaussian filter in space and time to the model output with a regionally varying temporal filter according to the determined periods, and a spatial filter of 4 to 20° longitude. For the mooring data, only temporal filtering is applied.

3.2. Mixing and Heat Flux Calculation

The potential for mixing is assessed via calculation of vertical shear of horizontal velocity $S^2 = \left(\frac{du}{dz}\right)^2 + \left(\frac{dv}{dz}\right)^2$ and reduced shear squared $S_{red}^2 = S^2 - 4N^2$, with N being the Brunt-Väisala-Frequency. Reduced shear squared S_{red}^2 relates to the Richardson number Ri which is an indicator for the likelihood of mixing in the ocean. For $S_{red}^2 > 0$, Richardson number $Ri < 0.25$ from which follows that the flow is more likely to be unstable and mixing can occur.

SubTIW-related vertical heat flux is calculated as $Q_w(z) = c[\overline{w(z)'T(z)'}]$ where primes denote subTIW temperature and velocity anomalies, overbar indicates time averaging and square brackets indicate horizontal averaging over the respective areas through which the flux is directed. $c = c_p \cdot \rho$ is the volumetric heat capacity and assumed to be constant (Cummins et al., 2016), with the specific heat of seawater $c_p = 3850 \frac{J}{kgK}$ and density of seawater $\rho = 1025 \frac{kg}{m^3}$. To assess the vertical heat flux in each region in the upper and lower thermocline separately, we calculate Q_w across a plane in the middle of the upper and lower thermocline, respectively. Hence, $Q_w(z_{upper}/2)$ describes the heat flux across a plane in the middle of the upper thermocline and $Q_w(z_{lower}/2)$ describes the heat flux across a plane in the middle of the lower thermocline. Equivalently, meridional and zonal heat flux are calculated as $Q_v(lat) = c[\overline{v(lat)'T(lat)'}]$ and $Q_u(lon) = c[\overline{u(lon)'T(lon)'}]$, respectively. We calculate the horizontal heat flux across each region by calculating Q_v and Q_u for a plane in the middle of the region, i.e., $Q_v(lat/2)$ and $Q_u(lon/2)$, for both upper and lower thermocline.

3.3. Calculating TIW and SubTIW Composites

Composite analysis allows for studying the impact of TIWs and subTIWs separately and for quantifying the relative importance of TIWs compared to subTIWs for vertical shear S^2, stratification N^2, horizontal heat flux Q_u, Q_v and vertical heat flux Q_w above the thermocline in all three regions. To calculate the composites, we adapt the approach described by Foltz et al. (2020): For each region, we define TIW energy as 15–60-day band-pass filtered $u'^2 + v'^2$ at the uppermost model layer, averaged over the respective regions.

Table 1
Depth Averaged Mean Values of Vertical Shear S^2, Stratification N^2 and Horizontal Heat Flux Q_u, Q_v in Region North and Region South, Calculated Using the Entire Time Series to Normalize the Composite Means

Region		$\mathbf{S^2}$ $[10^{-4} s^{-2}]$	$\mathbf{N^2}$ $[10^{-4} s^{-2}]$	$\mathbf{Q_u}$ $[10^4 Wm^{-2}]$	$\mathbf{Q_v}$ $[10^4 Wm^{-2}]$	$\mathbf{Q_w}$ $[Wm^{-2}]$
North	upper	0.4	3.8	5.7	−31.7	24
	lower	0.1	6.1	−6.3	−32.7	17
South	upper	1.5	1.8	0.9	2.5	3.9
	lower	0.3	4.1	9.0	6.8	3.5

Note. Mean values are separated into upper thermocline (7–40 m) means and lower thermocline (40–80 m) means. Vertical heat flux Q_w in each region is given as the time mean flux across a plane in the middle of the upper and lower thermocline, respectively.

Consequently, subTIW energy is defined as area averaged $u'^2 + v'^2$ in 64 m depth, band-pass filtered with the periods described in Section 3.1 for each region separately. As such, we gain a TIW and subTIW energy time series for each region. Values greater than one standard deviation above mean are considered high energy periods, values less than mean minus 40% of one standard deviation are considered low energy periods, following the definition by Foltz et al. (2020). All periods with high energy are combined to the composites for strong TIW and subTIW activity, all periods with low energy are combined to the composites for weak or no TIW and subTIW activity. We then compute mean composite values for each variable and region, averaged over the upper (7–40 m) and lower thermocline (40–80 m) separately. The composite mean is normalized by dividing the individual composite mean by the respective depth averaged mean over the entire time series. The mean values of vertical shear S^2, stratification N^2, horizontal heat flux Q_u, Q_v, and vertical heat flux Q_w in each region that were used to normalize the composite means are listed in Table 1. Normalized composite means of 1 indicate that the considered wave event does not alter the overall mean. Values larger than 1 indicate an increase in the respective variable due to the wave, while values less than 1 indicate a decrease caused by instability waves. We test for significance of the resulting composite means using bootstrapping methods. All shown values are significant on the 99% significance level.

4. Results

4.1. Comparison of Observed and Simulated Zonal Mean Flow Field

Ocean circulation in the tropical Atlantic Ocean is dominated by zonal currents, namely the SEC and NECC at the surface and the EUC at greater depths (Figure 3). These currents are of particular interest to our study as increased shear between the opposing currents can create instabilities which generate subTIWs. Hence, the realistic representation of these currents is a prerequisite for studying subTIWs in ICON-O. Therefore, we compare observations and model output of the equatorial flow field to show that ICON-O resolves the equatorial current system well. The long term mean zonal flow field over the 16- year simulation is shown in Figure 3. At the surface (Figure 3, top panel), the NECC can be seen as a clear eastward current north of approximately 4°N. Between the NECC and the Equator, the flow is directed westward by the SEC. The location and strength of both the SEC and NECC agree well with results from previous studies (Brandt et al., 2010; Lumpkin & Johnson, 2013; Perez et al., 2019) and suggest that ICON-O is able to create feasible current shear. At 64 m depth (Figure 3, bottom panel), the most prominent flow is the eastward EUC, located on the Equator in agreement with observations (Brandt et al., 2010). We further explore the simulation of the EUC by comparison of the simulated long term mean zonal velocity along 23°W with the mean zonal velocity observed during ship sections between 1999 and
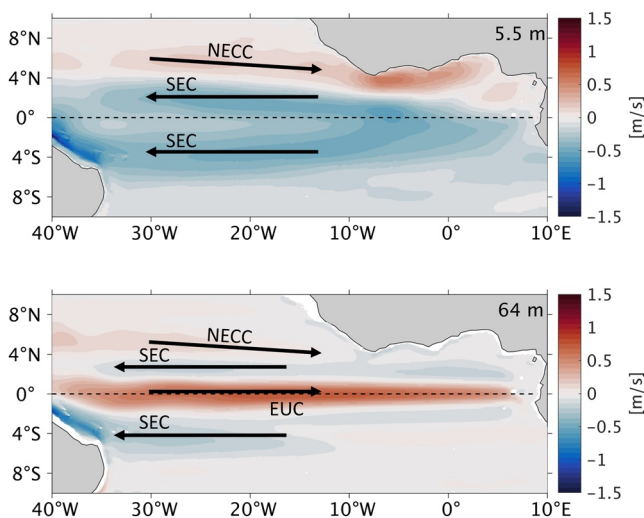

Figure 3. Simulated long term mean zonal velocity in the surface layer (5.5 m, top panel) and subsurface tropical instability waves (subTIW) layer (64 m, bottom panel). Velocities are given in m/s. Positive values indicate eastward velocities, negative values indicate westward velocities. Black arrows show a schematic of the dominant zonal currents in the respective depths. EUC: Equatorial Undercurrent; NECC: North Equatorial Countercurrent; SEC: South Equatorial Current.
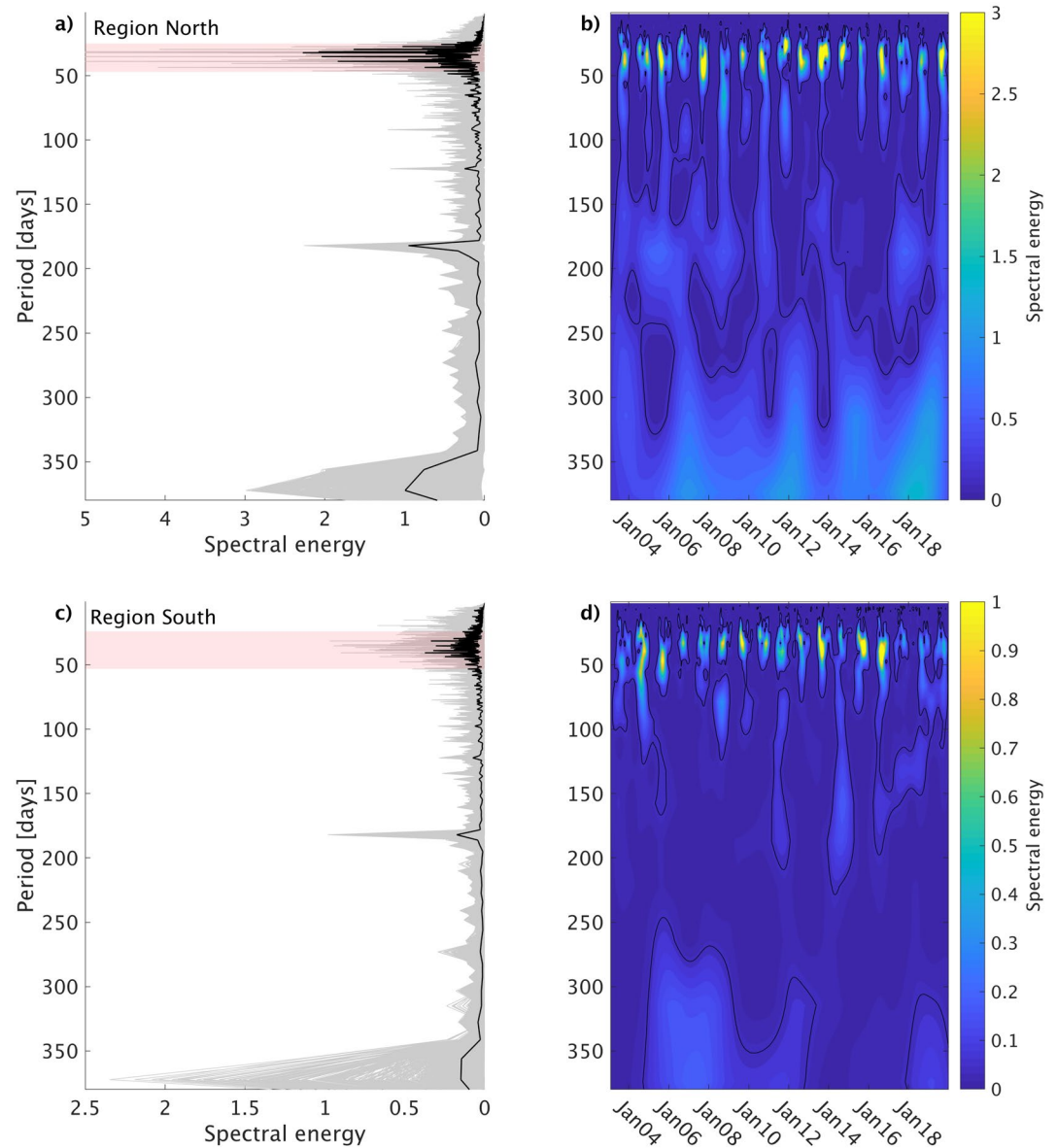
Figure 4. Power spectral density (a) and (c) and wavelet transforms (b) and (d) of simulated meridional velocity in 64 m depth in Region North (top panels, (a) and (b)) and Region South (bottom panels, (c) and (d)). Gray lines in (a) and (c) show power spectral density for each model grid point in the respective region. Thick black line indicates the box averaged power spectral density. Red shading shows the selected period window for subsurface tropical instability wave filtering. The wavelet transforms in (b) and (d) are calculated by averaging the wavelet transforms computed for each grid point in the respective regions. Black contours in (b) and (d) are the 95% confidence interval. It should be noted that the axis limits differ between Region North and Region South.

2008, presented in Brandt et al. (2010, Figure 2a therein). In these observations, the EUC extends from just below the surface to 200 m depth at 0°N, 23°W and spans a width from approximately −1.75°S to 1.75°N. The core (defined as the depth of the strongest eastward velocity) is located at the Equator in approximately 80 m depth. Zonal velocity profiles from the PIRATA mooring at 0°N, 23°W, averaged over the observation period (not shown) also show the EUC core depth at the Equator to be 75 m with a maximum zonal velocity of 0.8 m/s. In comparison, the simulated EUC ranges between −1.75°S and 1.5°N with its core depth at the Equator in approximately 70 m depth and a maximum zonal velocity of 1 m/s (not shown), hence comparable magnitude to the observations. Therefore, we conclude that ICON-O is able to simulate the equatorial zonal currents', in particular the EUC, characteristics sufficiently well to study subTIWs.

4.2. Simulated Velocity Variability in the SubTIW Period Band

We compute power spectral density and wavelet transforms of the simulated, unfiltered meridional velocity in 64 m depth to identify the dominant scales of current variability and their relative strength in the subTIW dominated regions Region North and Region South. In particular, we assess the importance of variability on subTIW time scales.Spectral energy of meridional velocity in both Region North (Figure 4a) and Region South (Figure 4c) is high around periods of one year and 180 days, highlighting the strength of the annual and semiannual cycle in the tropical Atlantic (Brandt et al., 2016). Furthermore, in both regions, spectral energy of meridional velocity peaks in the intraseasonal band (less than approximately 100 days), in particular at periods less than 60 days. This can be explained by the presence of subTIWs and highlights the importance of subTIWs for meridional current variability. The strength of the intraseasonal variability compared to the semiannual and annual cycle varies within the regions (gray lines in Figures 4a and 4c). At individual points, intraseasonal variability is the strongest source of variability while others are dominated by the annual or semiannual cycle. In Region North, the intraseasonal signal can even largely exceed the otherwise strong annual cycle (Figure 4a). However, when considering the entire regions, indicated by the black lines in Figures 4a and 4c, intraseasonal variability is the leading mode of variability. Regionally averaged power spectral density in the intraseasonal period band is about twice as strong as the semiannual and annual variability in both regions. It should be noted that Region North and Region South were chosen due to high subTIW occurrence and consequently intraseasonal variability in these two regions is stronger compared to other regions of the tropical Atlantic. Therefore, this result is not representative for the entire tropical Atlantic, where the semiannual and annual cycle are the dominant source of variability (Brandt et al., 2016).

Since subTIW occurrence is a seasonal phenomenon, their strength may further be underestimated when only considering power spectral density over the entire simulation period. Therefore, we also compute wavelet transforms of the meridional velocity, which allow for including the seasonal character of subTIWs in the analysis. These are shown in Figures 4b and 4d. Here, a clear pattern of high spectral energy in boreal autumn and winter in the subTIW period band can be seen in both regions, which largely exceeds the mean energy in other period bands. This indicates that high energy in the intraseasonal period band is indeed caused by subTIWs.

In conclusion, analysis of power spectral density and wavelet transforms shows that in the identified regions energy in the intraseasonal period band is the leading mode of variability which is further enhanced during boreal autumn and winter when subTIWs typically occur. Hence, subTIWs can be considered an important source of current variability. Last, it should be noted that while the relative importance of intraseasonal variability is comparable in both regions, spectral energy is overall higher across all scales of variability in Region North compared to Region South.

4.3. SubTIW Activity in Simulations and Observations at PIRATA Mooring Sites

In this section, we show that subTIWs can be identified at both PIRATA mooring locations with distinct subsurface velocity maxima in both velocity components. To assess model accuracy in simulating this activity, we compare observed velocities with the corresponding model output.

4.3.1. 4°N, 23°W

At 4°N, 23°W, observed subTIW-associated (30–45 days band-pass filtered) meridional velocity in 67 m depth shows three subTIWs between June and August 2017 (Figure 5). Two less pronounced subTIWs can be found in November and December. We do not compare the observations directly to the respective simulation year because we expect the simulation to have its own variability. Therefore, we cannot assume the agreement of simulation and observations in a specific year. Looking at all 16 simulation years in Figure 5 (blue dotted lines) reveals that subTIWs undergo pronounced year-to-year variability. Simulated subTIWs are most pronounced in boreal summer, in agreement with the observations, but can occur until February of the following year with decreasing velocity amplitudes. Throughout the whole simulation period, subTIW amplitudes reach a maximum of about 20 cm/s, compared to the observed maximum velocity amplitude of 24 cm/s. Highlighting the simulated period from March 2004 to March 2005 (solid blue line in Figure 5) shows that the ICON-O can very well reproduce variability such as the observed subTIWs.
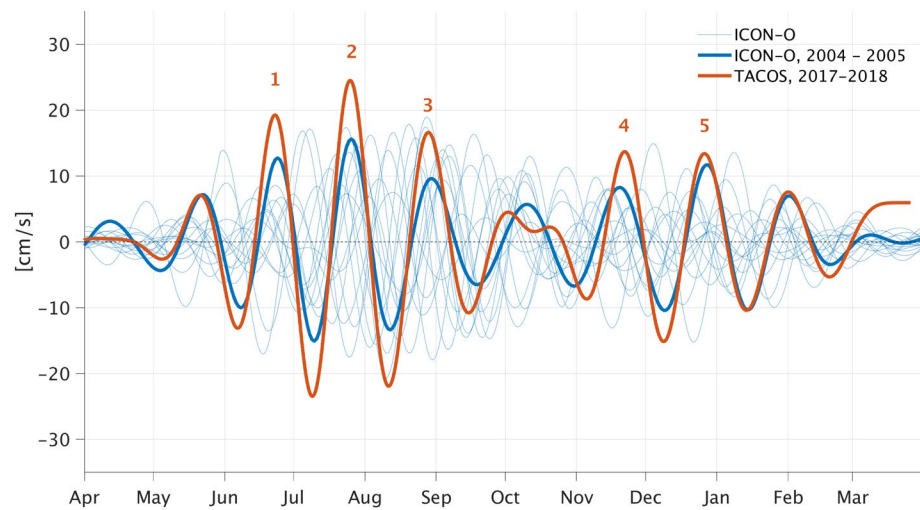
Figure 5. Subsurface tropical instability waves (subTIW)-associated meridional subsurface velocity at 4°N, 23°W in ICON-O for all 16 simulation years (blue dotted lines) and observed subTIW-associated meridional velocities at the Tropical Atlantic Current Observation Study (TACOS) mooring site (orange) from March 2017 to March 2018. The solid blue line shows simulated meridional velocities from March 2004 until March 2005. The temporal filter for both observations and simulation is 30–45 days. Orange numbers indicate subTIWs observed at the TACOS mooring site. Observed meridional velocity are shown for 67 m depth, simulated meridional velocity is shown for 64 m depth.

Applying a 30–45-day band-pass filter to the observed velocity reveals subsurface velocity maxima at 4°N, 23°W in both horizontal and zonal velocity components (Figures 6a and 6b). Meridional velocity is strongest between 46 and 67 m depth from June to September. A secondary subsurface maximum is located between 32 and 62 m depth from November to January. In comparison, the zonal velocity subsurface maximum is located between 44 and 67 m from June to September and at 30–58 m depth from November to January. However, the subsurface velocity maxima in boreal summer are located at the greatest observed depth level. We cannot rule out that velocities are even larger at greater depth.
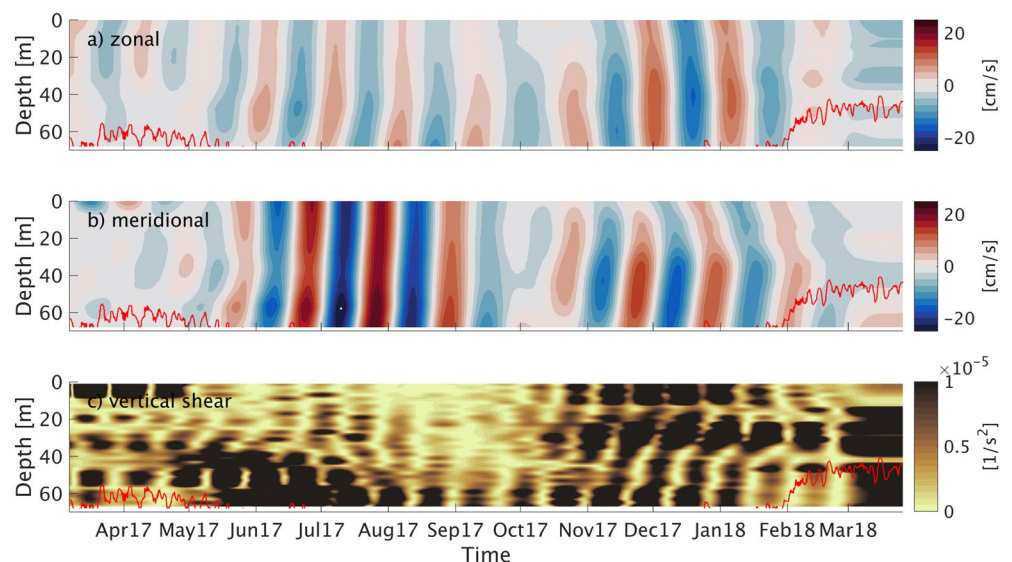

Figure 6. Observed 30–45-day band-pass filtered zonal velocity ((a), top panel), meridional velocity ((b), middle panel) and vertical shear squared $S^2 = \left(\dfrac{du'}{dz}\right)^2 + \left(\dfrac{dv'}{dz}\right)^2$ ((c), bottom panel) at 4°N, 23°W. Velocities are given in cm/s, vertical shear is given in $1/s^2$. Positive velocities indicate eastward and northward flow. Negative velocities indicate westward and southward flow. The red line represents the thermocline depth (20° isotherm).
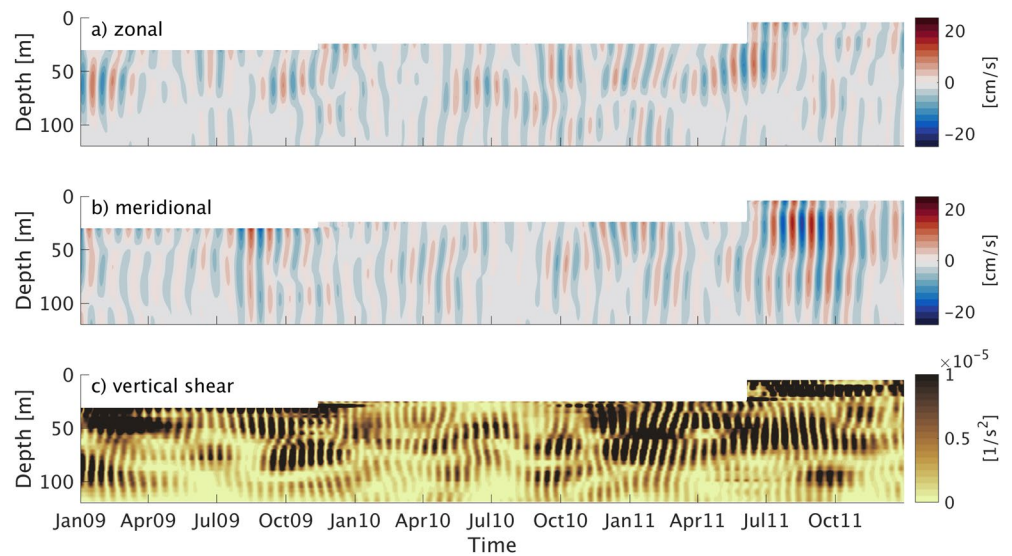
Figure 7. Observed 24–30-day band-pass filtered zonal velocity ((a), top panel), meridional velocity ((b), middle panel) and vertical shear squared $S^2 = \left(\dfrac{du'}{dz}\right)^2 + \left(\dfrac{dv'}{dz}\right)^2$ ((c), bottom panel) at 0°N, 23°W from January 2009 to January 2012. Velocities are given in *cm/s*, vertical shear is given in $1/s^2$. Positive velocities indicate eastward and northward flow. Negative velocities indicate westward and southward flow.

Both zonal and meridional subsurface velocity anomalies reach amplitudes of about 15 cm/s during November to January. However, in boreal summer, the meridional subsurface velocity anomaly is the dominant component with up to 25 cm/s compared to 10 cm/s for the zonal component. Furthermore, similar to the two-layer shear structure described in Liu et al. (2019), observed vertical shear exhibits a vertically complex multilayer structure during the times of subTIW occurrence, with increased S^2 in the depths of the subsurface velocity maxima. Such vertically complex multilayer shear structure is not visible when applying a filter of 15–60 days, which are the characteristic periods of TIWs.

4.3.2. 0°N, 23°W

At 0°N, 23°W, several years of observations are available in 65 m depth, which allow for a more reliable comparison. Observed subTIW-associated (26–30 days band-pass filtered) subsurface meridional velocity oscillations are strongest in August and September with amplitudes of up to 9 cm/s. Simulated subTIW-associated subsurface velocity oscillations are of comparable magnitude. However, strongest oscillations occur in July and August. The observed subTIW-associated zonal subsurface velocity shows strong year-to-year variability. Oscillations with a magnitude of up to 8 cm/s can occur in any month. In comparison, subTIW zonal subsurface velocity oscillations in ICON-O are strongest between August and the following March, with amplitudes of the same magnitude as the observed velocity oscillations.

Analysis of observed velocities in the subTIW period band (26–30 days) shows subsurface zonal velocity anomaly maxima at varying depths between 60 and 100 m, with an amplitude of 6 cm/s on average (Figure 7a). Subsurface meridional velocity anomaly peaks at 66 m depth on average with an amplitude of approximately 9 cm/s (Figure 7b). Vertical shear features a vertically complex multilayer structure (Figure 7c), which resembles the two-layer shear structure described in Liu et al. (2019), particularly during 2010.

Different from the findings in the equatorial Pacific by Liu et al. (2019), subTIWs in the Atlantic are not solely manifested in subsurface velocity oscillations of the zonal velocity component. Instead, subsurface maxima can be found in both zonal and meridional velocities, with stronger amplitudes found in the meridional component. The latter is particularly true for the mooring north of the Equator, which can be explained by the decreasing strength of the zonal EUC away from the Equator and an increasing role of meridional velocities. When comparing the two mooring locations, subsurface velocity maxima are overall less pronounced at the Equator than to the north, suggesting stronger subTIW activity off the Equator.
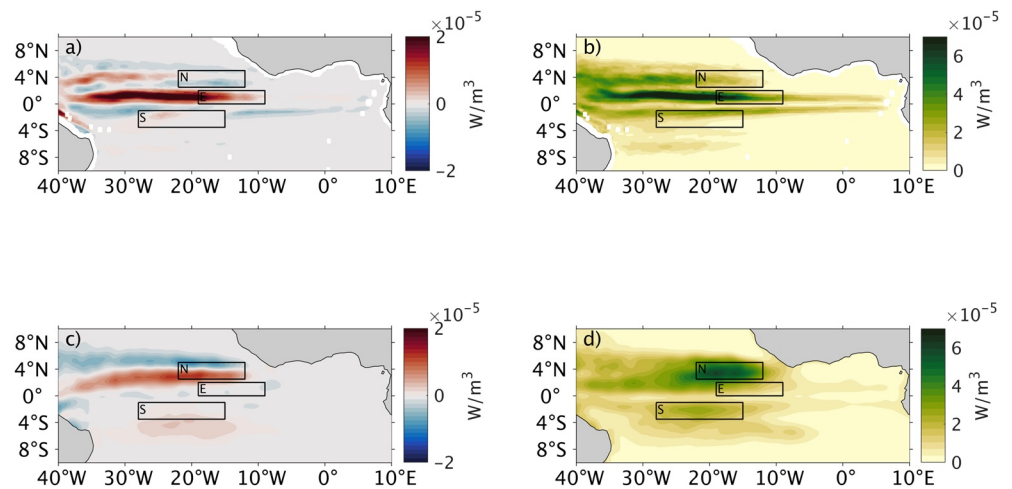
Figure 8. Barotropic ((a and b), upper panels) and baroclinic ((c and d), bottom panels) conversion rates in 64 m depth in W/m^3 (a) and (c) show the mean conversion rates overall simulated subsurface tropical instability wave (subTIW) seasons (May–November of each simulation year). Positive values indicate that energy is being fed into the instability. Negative values indicate that energy is being transferred back into the mean circulation. (b) and (d) show the standard deviation of the conversion rates overall simulated subTIW seasons.

4.4. Generation Mechanisms of SubTIWs in ICON-O

Next, we take advantage of the global model domain of ICON-O to investigate the generation mechanisms of subTIWs. Such analyses are not possible with single spot moorings alone. We find that subTIWs are generated both north and south of the Equator through both baroclinic and barotropic conversion, with a larger contribution of baroclinic energy conversion. In particular north of the Equator, baroclinic energy conversion leads to subTIW generation, while barotropic energy conversion feeds energy back into the mean circulation.

To study the generation mechanisms of subTIWs, we have a closer look at the eddy kinetic energy. We compute the so called barotropic and baroclinic energy conversion terms. This approach is similar to the one first used by Masina et al. (1999) to investigate the generation of surface-intensified TIWs and which has since been repeatedly used to study the generation of TIWs (e.g., de Decco et al., 2018; Jochum et al., 2004; von Schuckmann et al., 2008). Barotropic energy conversion describes the production and destruction of eddy kinetic energy due to the horizontal shear of the mean flow. Baroclinic energy conversion shows the conversion of eddy available potential energy into eddy kinetic energy and vice versa. Hence, barotropic and baroclinic conversion terms show energy conversion related to horizontal and vertical shear instabilities. Such instabilities can be manifold, in particular in complex flow structures like the equatorial current system, for example, barotropic and baroclinic instabilities, as well as Kelvin-Helmholtz instabilities and over-reflection (Proehl, 1996). Here, we focus on analyzing the generation of subTIWs in terms of energy conversion rates and do not give a detailed description of all possible involved instabilities. As in (Jochum et al., 2004) we refer to barotropic and baroclinic instabilities, based on the underlying barotropic and baroclinic energy conversion. Barotropic energy conversion is calculated as $bar_{conv} = -\rho_0 \overline{u'v'} \frac{\partial U}{\partial y}$, with U the annual mean zonal velocity and u', v' the 15–60-day filtered velocities. Baroclinic energy is calculated as $barclin_{conv} = -g\overline{\rho'w'}$, with w' the 15–60-day filtered vertical velocity and ρ' the 15–60-day filtered density. We are aware that our approach shows the energy exchange between the background state and intraseasonal processes in general and may as such also include intraseasonal processes other than subTIWs. However, as previously discussed in Section 4.2, subTIWs are the main source of intra-seasonal variability in 64 m depth. Hence, it can be assumed that the calculated energy conversion is primarily between the background state and subTIWs and can therefore be used to explain the generation of subTIWs in 64 m depth. The top panels of Figure 8 show the mean barotropic conversion rate (a) and its standard deviation (b) in 64 m depth, calculated overall simulated subTIWs periods. The bottom panels of Figure 8 show the mean baroclinic
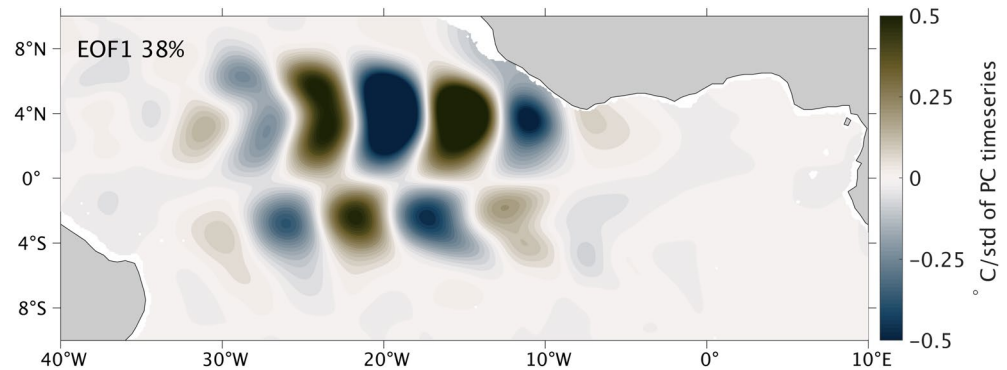
Figure 9. First empirical orthogonal function (EOF) mode of the 15–60-day filtered simulated temperature in 64 m depth and the explained variance. The pattern is shown as a regression map, using the principal component 1 (PC1) time series. The time series was normalized to unit variance prior to the regression. The EOF1 regression map shows values as °C/standard deviation of PC1 time series.

conversion rate (c) and its standard deviation (d) in 64 m depth, calculated overall simulated subTIWs periods. Both mean baroclinic and barotropic conversion are of comparable magnitude (O ($10^{-5} W/m^3$), Figures 8a and 8c), suggesting that horizontal and vertical shear instabilities play a role in generating subTIWs. The mean barotropic and baroclinic conversion rate south of the Equator is small but positive, meaning that energy is transferred into the instability through both barotropic and baroclinic energy conversion. Despite the small mean conversion rate values, standard deviation of both baroclinic and barotropic conversion is increased south of the Equator. In particular, standard deviation of the baroclinic conversion shows a maximum in Region South, which suggests mean values with high variance. Strongest standard deviation of baroclinic conversion can be found in Region North. There, mean baroclinic conversion values are both positive and negative which implies that energy is transferred both into subTIWs as well as back into the mean current. In comparison, barotropic energy conversion is negative in Region North, implying that energy is being transferred from the instability back into the mean circulation. This suggests that in Region North, generation of subTIWs is mainly caused by baroclinic energy conversion. Barotropic energy conversion is high between the Equator and 2°N, west of 10°W. However, in this region, subTIWs rarely occur which suggests that the barotropic energy conversion feeds energy into perturbations other than subTIWs. It is unclear, why the baroclinic conversion in the subsurface is high in the western basin, north of 3°N, where subTIWs cannot be found. This question needs further investigation, which, however, is not part of the main scope of this study.

Following from the simulated mean zonal flow field (Figure 3, bottom panel), we suggest that shear instabilities related to subTIW generation in the southern hemisphere, stem from shear between the southern flank of the EUC and the mean westward current south of it. The EUC intensifies in boreal summer and autumn with an observed maximum in July–September (Hormann & Brandt, 2007) which leads to increased shear between the EUC and the SEC, as such providing forcing for subTIWs. On the other hand, in the northern hemisphere, instabilities are most likely generated by shear between the SEC and NECC.

4.5. Spatial Extent of Simulated SubTIWs

We conduct an empirical orthogonal function (EOF) analysis to study the dominant subTIW spatial pattern. Our results suggest that, unlike known from TIWs, subTIWs are frequently present on both sides of the Equator.

Since subTIWs are propagating waves, the wave pattern is characterized by pairs of EOFs (Wang et al., 2020). The first four EOF modes of the 15–60-day filtered simulated temperature in 64 m depth, which only differ in their sign and are shifted by $\pi / 2$, respectively, together explain about 85% of the total variance. To focus on the spatial pattern, rather than the propagation of the wave, Figure 9 shows the first EOF mode, which explains about 38% of the total variance. The EOF in Figure 9 is presented as a regression map, using the normalized first principal component (PC) time series. The PC1 time series is normalized to unit variance.
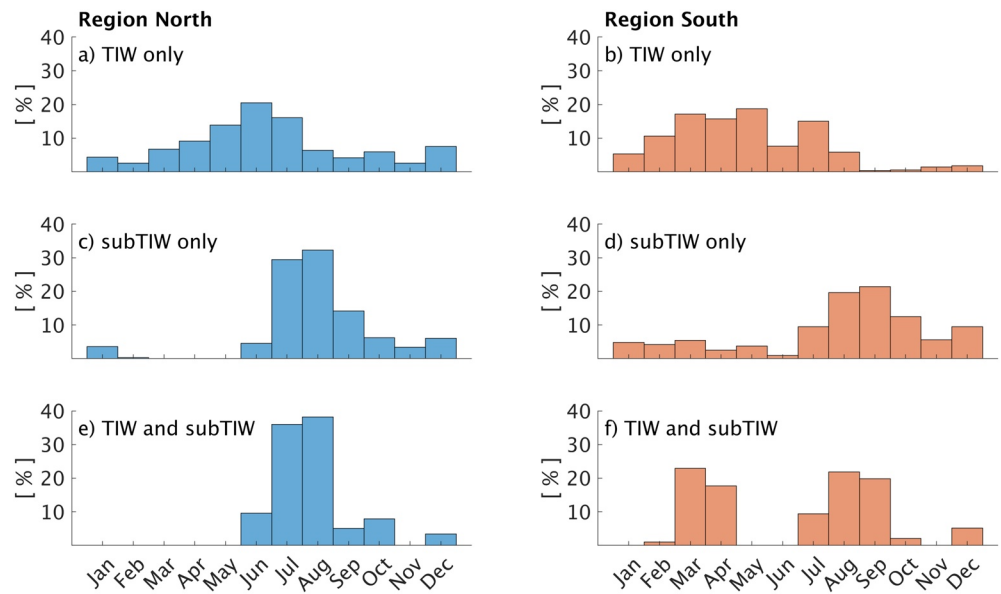
Figure 10. Histograms of tropical instability wave (TIW) and subsurface tropical instability wave (subTIW) occurence in Region North (left) and Region South (right), based on daily model output and calculated for the entire simulation period. TIW and subTIW occurrences in the respective months are shown as percentage of the total amount of occurrences. (a) and (b) show the occurrence of only TIWs. (c) and (d) show the occurrence of only subTIWs. (e) and (f) show the simultaneous occurrence of TIWs and subTIWs.

Hence, the pattern illustrates the change of temperature in °C per standard deviation of the normalized PC time series.

An oscillating temperature pattern is apparent in both hemispheres, mirrored around the core of the EUC on the Equator. This confirms the existence of subTIWs both north and south of the Equator. However, the pattern is not symmetric around the Equator. In the northern hemisphere, the subTIW related temperature pattern expands as far as 8°N, while in the southern hemisphere it is limited to 5°S, suggesting a larger region of subTIW influence in the northern hemisphere. Such pattern is distinctively different from the characteristic temperature pattern caused by surface-intensified TIWs, which is concentrated exclusively north of the Equator as shown for example in de Decco et al. (2018, Figure 4 therein).

4.6. Regional Differences in SubTIWs Characteristics in ICON-O

In the following, we investigate the spatial differences of subTIWs by focusing on the wave characteristics in Region North and Region South. In both regions, we find subTIWs to be strongest between approximately 30 and 90 m depth with an average occurrence time approximately three months later than surface-intensified TIWs in Region South and one month later in Region North.

4.6.1. Region North

In Region North, subTIWs occur between June and January of the following year. Most pronounced subTIW activity is found in July and August (Figure 10c). During these months, subTIWs and surface-intensified TIWs can also frequently occur simultaneously (Figure 10e). Figure 11 illustrates simulated horizontal velocities, vertical shear and reduced shear squared in 2013. Despite showing results for only one year, our analyses consider the entire simulation period. Thus, the mentioned values in the following refer to the full simulation period and may differ from the values seen in Figure 11.

SubTIWs occur between 32 and 75 m depth, visible as subsurface velocity maxima. Meridional velocities peak at approximately 61 m depth with an average velocity amplitude of about 4.1 cm/s. The velocity magnitudes are likely to be smaller than the observed velocities at the mooring site because we consider box averaged simulated velocities for the regional analysis. S^2 and N^2 were calculated for each grid point before
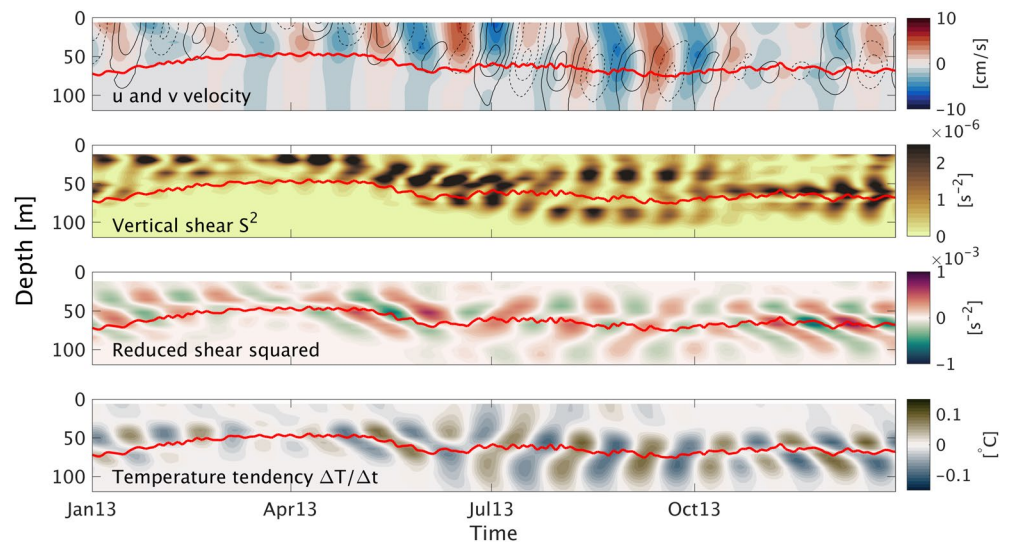
Figure 11. Simulated 24–53-day filtered horizontal velocity, vertical shear S^2, reduced shear squared and temperature tendency $\Delta T / \Delta t$ in year 2013 in Region North. Vertical shear S^2 and reduced shear squared S^2_{red} are calculated using subsurface tropical instability wave (subTIW) velocity anomalies u' and v'. Top panel: Zonal velocity u shown in shading in cm/s. Positive values indicate eastward flow, and negative values indicate westward flow. Meridional velocity v is shown in contours with contour spacing of 2 cm/s. Dashed lines indicate southward velocities, and solid lines indicate northward velocities. Second panel: Vertical shear S^2. Third panel: Reduced shear squared S^2_{red}. Positive values indicate unstable flow conditions. Bottom panel: Temperature tendency $\Delta T / \Delta t$, with T being temperature in °C and t being time in days. The red line in all plots shows the thermocline depth (20°C isotherm).

calculating the regional average. Zonal velocities exhibit less frequent subsurface maxima at an average depth of 59 m. However, the amplitude of the zonal subsurface velocity maxima is about 2.6 cm/s on average and thus two thirds as strong as the meridional maxima. This points to the importance of the meridional velocity component for subTIWs north of the Equator. Shear squared S^2 exhibits a vertical two-layer structure during periods of subTIW activity with alternating shear maxima below and above the subsurface velocity peaks. This is a feature which cannot be found when applying a wider temporal band-pass filter, such as filtering for TIWs. Thus, the two-layer shear structure appears to be a unique feature of subTIWs. Liu et al. (2019) state that such vertical shear structure caused by subTIWs to be responsible for altered vertical mixing compared the mixing occurring during TIW only periods or times of absence of instability waves. Reduced shear squared $S^2_{red} = S^2 - 4N^2$, which is a measure for vertical flow stability, exhibits an oscillating pattern similar to the vertical shear pattern. During the first half of the year, S^2_{red} is enhanced close to the surface, indicating the effect of surface intensified TIWs. However, from May onward S^2_{red} is stronger below 40 m. In particular, after June S^2_{red} exhibits an oscillating pattern just below and above the thermocline, coinciding with the surface velocity maxima, while close to the surface S^2_{red} vanishes. This supports the idea that the specific vertical shear structure caused by subTIWs, which differs from the periods when subTIWs are absent, destabilizes the flow in the subsurface and thereby may enhance vertical mixing.

4.6.2. Region South

In Region South, subTIWs can occur all year round. However, they are most frequently present in August and September (Figure 10d). During this period, they can also occur simultaneously with TIWs (Figure 10f). Again, we only show results for 2013 in Figure 12, despite considering the entire simulation period for the analysis.

In Region South, subTIWs occur between 29 and 94 m depth. However, unlike in Region North, in Region South, subsurface velocity maxima most often occur in the zonal velocity component. Zonal velocity peaks in an average depth of 67 m with a velocity amplitude of 4 m/s. In comparison, meridional velocity peaks in 50 m depth with an average amplitude of 4.1 m/s. Hence, meridional velocity subsurface maxima are of comparable magnitude to Region North, while zonal velocity subsurface maxima are about 50% stronger in Region South. Comparable to Region North, a two-layer vertical shear structure is apparent. It is
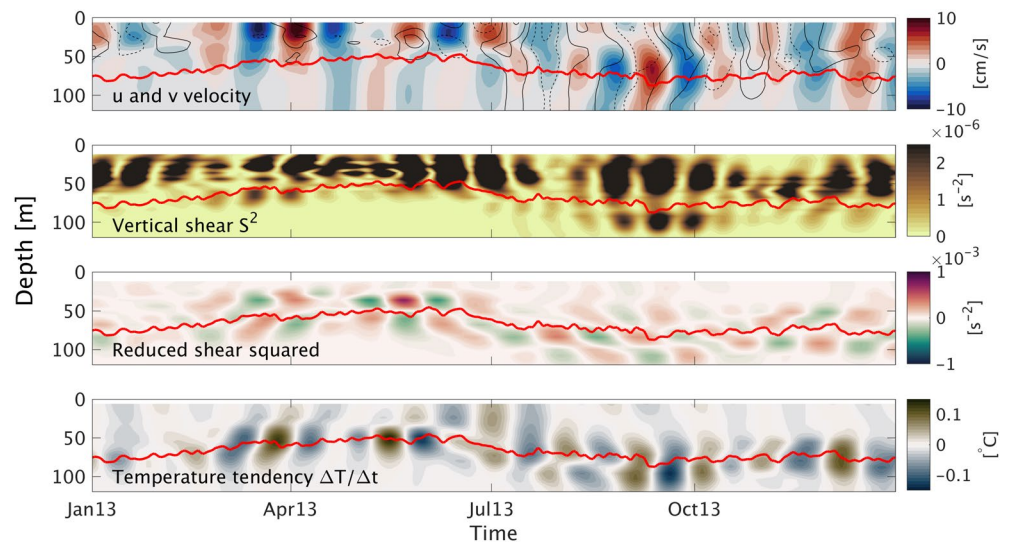
Figure 12. Simulated 25–47-day filtered horizontal velocity, vertical shear S^2, reduced shear squared and temperature tendency $\Delta T/\Delta t$ in year 2013 in Region South. Vertical shear S^2 and reduced shear squared S^2_{red} are calculated using subsurface tropical instability wave velocity anomalies u' and v'. Top panel: Zonal velocity u shown in shading in cm/s. Positive values indicate eastward flow, negative values indicate westward flow. Meridional velocity v is shown in contours with contour spacing of 2 cm/s. Dashed lines indicate southward velocities, and solid lines indicate northward velocities. Second panel: Vertical shear S^2. Third panel: Reduced shear squared S^2_{red}. Positive values indicate unstable flow conditions. Bottom panel: Temperature tendency $\Delta T/\Delta t$, with T being temperature in $°C$ and t being time in days. The red line in all plots shows the thermocline depth (20°C isotherm).

particularly pronounced from August onward, with maxima below and above the subsurface zonal velocity maxima, suggesting that subTIWs cause the vertical shear pattern. In comparison, S^2_{red} is smaller than in Region North. Strongest oscillations can be found in boreal spring, coinciding with near surface velocity maxima. In contrast, during periods of subTIW occurrence S^2_{red} amplitudes are smaller. Nonetheless, values of S^2_{red} become positive when subTIWs are present. This indicates the potential of subTIWs to destabilize the mean flow in Region South, despite this effect being weaker than that north of the Equator.

4.7. Regional Differences in SubTIW Impact on Vertical Mixing and Heat Flux in ICON-O

To assess the regional differences in subTIW impact on vertical mixing and heat flux, we conduct a composite analysis for each region separately. The results of the composite analysis are shown in Figure 13. We also include TIWs in the composite analysis to evaluate the impact of subTIWs relative to the impact of TIWs. We find that in both Region North and Region South, subTIWs impact vertical mixing and heat flux. Despite the relative influence of subTIWs often being smaller than the changes caused by TIWs, subTIWs lead to a significant contribution in altering mixing and heat fluxes in the thermocline. Furthermore, we find that heat flux is affected most strongly when both TIWs and subTIWs occur simultaneously, which suggests that the interaction of the two waves is of major importance for the thermocline dynamics.

In Region North, both TIWs and subTIWs increase vertical shear S^2 throughout the entire thermocline. TIWs lead to a shear increase of approximately 40% while subTIWs increase shear by 20% (Figures 13a and 13c). The combined effect on shear is of comparable magnitude to the one from TIWs alone. In Region South, in the upper thermocline (Figure 13a), TIWs and subTIWs have an opposing effect on vertical shear. While TIWs increase shear by 20%, subTIWs decrease shear by the same amount. However, in the lower thermocline (Figure 13c), TIWs do not impact vertical shear, while subTIWs cause a shear increase of 10%.

In the lower thermocline, stratification N^2 is only marginally altered by either of the wave types by approximately ±10% (Figure 13c). On the other hand, in the upper thermocline (Figure 13a), subTIWs decrease stratification in Region North and Region South by 60% and 20%, respectively. In Region North, TIWs lead
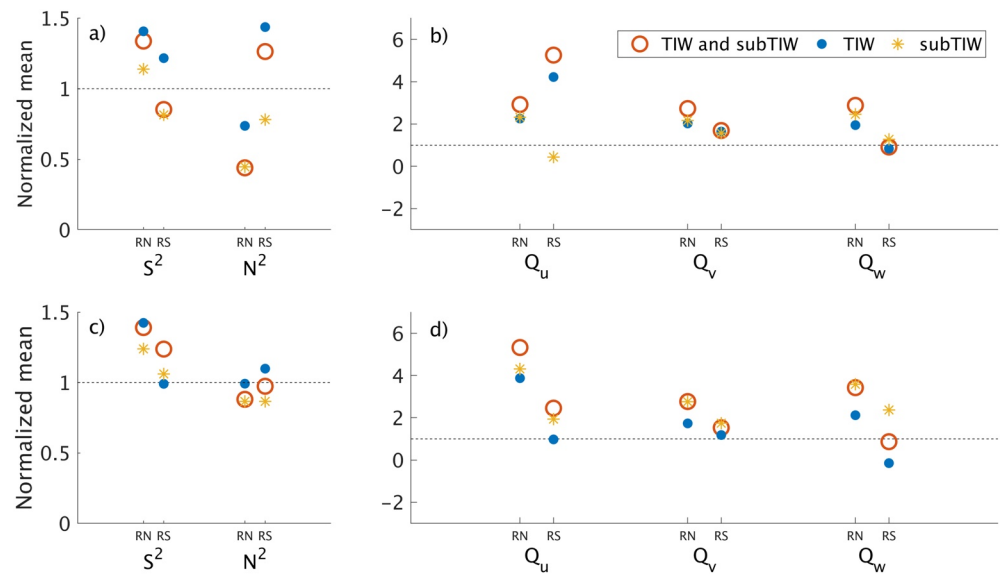
Figure 13. Composite analysis for strong tropical instability wave (TIW) (blue dot) and subsurface tropical instability wave (subTIW) (yellow cross) events and simultaneous occurrence of both (red circle) in the upper (a) and (b) and lower thermocline (c) and (d). Analysis is based on the model output. Upper thermocline includes the upper 40 m, lower thermocline includes 40–80 m. RN and RS indicate values for Region North and Region South. S^2: vertical shear; N^2: static stability; Q_u: zonal heat flux; Q_v: meridional heat flux; Q_w: vertical heat flux. All values are depth averaged means for the respective composites, normalized by the depth averaged mean of the full time series. The means are listed in Table 1.

to a smaller stratification decrease of 30%, while in Region South, TIWs increase stratification by 40%, again opposing the effect of subTIWs in this region.

In the upper thermocline, strongest effects on horizontal and vertical heat fluxes occur when TIWs and subTIWs are present simultaneously (Figure 13a). In Region South, zonal heat flux is strongly increased by TIWs, while subTIWs lead to a decrease. In Region North, both TIWs and subTIWs lead to a doubling in zonal heat flux. Meridional heat flux is increased by the same amount by both TIWs and subTIWs. Vertical heat flux is affected more strongly by subTIWs than TIWs. In fact, in Region South, no impact of TIWs alone on the vertical heat flux in the upper thermocline can be found. Also in the lower thermocline, the combined effect of TIWs and subTIWs generally has the largest effect on all heat flux components (Figure 13d). Furthermore, heat flux increase caused by subTIWs is stronger than the increase caused by TIWs, which was expected since subTIWs occur below 40 m.

We can relate subTIWs to temperature changes above the thermocline by analyzing the temperature tendency $\Delta T / \Delta t$ of the subTIW filtered temperature, shown in the bottom panels of Figures 11 and 12. In both Region North and Region South, the temperature tendency is strong around the thermocline depth. Temperature tendency is further increased during times of subTIW occurrence and generally coincides with increased vertical shear, suggesting an effect of subTIW and the induced changes in vertical shear on the thermocline temperature. Furthermore, temperature tendency is the strongest below approximately 50 m depth, which highlights the importance of subsurface dynamics compared to surface intensified TIWs. To quantitatively assess what the TIW and subTIW-induced changes in vertical shear, stratification and heat fluxes imply for the temperature above the thermocline, a detailed heat budget analysis would be necessary. However, such analysis is beyond the scope of the present work.

5. Distinction Between TIWs and SubTIWs

Previous studies (e.g., Perez et al., 2019) investigated TIWs in the tropical Atlantic and also considered the vertical extent of TIWs. In particular, Perez et al. (2019) find subsurface maxima of both mean zonal and meridional velocity in 32–47 m depth and 57 m depth, respectively, at the TACOS mooring site at 4°N,

23°W in the observational data used in our study as well. Furthermore, they find meridional velocities with amplitudes >60 cm/s reaching down to 67 m depth and perturbations with velocity amplitudes as large as 40 cm/s reaching down to 87 m depth. However, these studies do not distinguish between waves with different frequencies in the subsurface and consider velocity perturbations at depth to be a signal of TIW downward energy propagation. In the present study, we show that there are velocity oscillations in the sub-surface with shorter periods compared to TIWs which, when taken into account in the choice of temporal band-pass filter, reveal impact on vertical shear which differs from the one associated with TIWs. We argue that such subTIWs are a feature of the equatorial Atlantic, independent of and distinguishable from TIWs, rather than a depth expression of downward propagating surface-intensified TIWs. We base this conclusion on several findings from this study, namely the differences in occurrence time, spatial distribution and share of baroclinic and barotropic energy conversion in the wave generation. While TIWs develop mainly from May onwards (Figures 10a and 10b) in response to an intensification of the surface currents, development of subTIWs is strongest in July to September (Figures 10c and 10d), likely due to an intensification of the EUC between July and September (Hormann & Brandt, 2007) which increases the shear between EUC and SEC in the subsurface. SubTIWs can also occur in years when TIWs are absent. Furthermore, TIWs are predominantly located north of the Equator, whereas subTIWs are present away from the Equator in both hemispheres. The region of strongest TIW activity at the surface in ICON-O is highlighted in Figure 2, called the Region Equator. The region is obtained by applying the methods described in Section 3.1 to simulated surface temperature. In addition, the TIW spatial pattern can clearly be seen in the results from EOF analysis of surface temperature. Such analysis reveals an oscillating temperature pattern north of the Equator, comparable to the results from de Decco et al. (2018, Figure 4 therein). Such pattern is in contrast with the spatial pattern of subTIWs that we found in our study (Figure 9). Last, previous studies argue that TIWs north of the Equator are mainly generated by barotropic energy conversion due to instabilities of the mean zonal surface currents. In contrast, our results suggest that subTIWs are generated by both barotropic and baroclinic energy conversion in Region South and mainly by baroclinic energy conversion in Region North. However, it should be noted that our analysis does not allow for conclusions regarding the types of instabilities involved in the energy conversion.

6. Summary and Conclusion

The presence of subTIWs and their influence on vertical mixing in the tropical Atlantic were investigated using observation data from two PIRATA moorings and the high-resolution model output from the comprehensive, global, ocean model ICON-O. We identified subTIWs in observations in the Atlantic Ocean for the first time and studied their spatial distribution and regionally differing effect on mixing and heat flux using a high-resolution ICON-O simulation.

SubTIWs in both model and observations occur between approximately 30 and 90 m depth and manifest themselves as subsurface velocity peaks. SubTIWs north of the Equator are predominately expressed by oscillations of the meridional velocity component; to the south, the zonal velocity component is of greater relevance. SubTIWs mostly occur from June to December, with a maximum in July to September. In general, subTIWs begin to form approximately one to three months later than TIWs in response to EUC intensification, however, due to the strong year-to-year variability of both TIWs and subTIWs, they can also occur simultaneously. One of the most distinct differences between TIWs and subTIWs is the spatial extent. While TIWs primarily exist north of the Equator, subTIWs exhibit a mirrored pattern around the Equator with centers of high subTIW activity to both the north and south. SubTIWs induce a multilayer shear structure with shear maxima below and above the subsurface velocity maximum in both model and observations, which agrees with observations in the tropical Pacific Ocean from Liu et al. (2019). This oscillating shear pattern in the subsurface ocean shows the potential of subTIWs to destabilize the mean flow and thereby inducing mixing, shown by positive values of reduced shear squared above the thermocline. We show the relevance of subTIWs in relation to TIWs using a composite analysis of strong TIW and subTIW events. The results suggest great importance of simultaneous occurrence of both TIWs and subTIWs for vertical mixing and heat fluxes in the thermocline.

We conclude that subTIWs are a feature of the tropical Atlantic which impact vertical mixing and heat flux in the thermocline in two regions north and south of the Equator. Despite sharing similar characteristics

and time of occurrence, subTIWs appear to be independent of TIWs. Most evidently, subTIWs occur in different regions than TIWs. Due to the influence of subTIWs on upper ocean mixing and heat flux, future assessment of upper ocean heat budget and regional air-sea interactions should not be limited to the effect of TIWs alone. Instead, the impact of subTIWs should also be taken into account, particularly in the regions north and south of the Equator which are strongly affected by subTIWs. To date, it is not clear how subTIWs and TIWs interact, and it is unclear whether subTIWs only act in the subsurface or if they also have an impact on SST patterns, comparable to TIWs. However, these questions are crucial to fully understand the role and importance of subTIWs for the upper ocean and air-sea interactions and should therefore be addressed in future research.

Data Availability Statement

This study has been conducted using mooring data from the PIRATA project provided by the GTMBA Project Office of NOAA/PMEL. PIRATA and TACOS data can be obtained at the NOAA Pacific Marine Environmental Laboratory (PMEL) website (https://www.pmel.noaa.gov/gtmba/pirata). ICON-O primary data and scripts used in the analysis and other supporting information that may be useful in reproducing the author's work is archived by the Max Planck Institute for Meteorology in the MPG.PuRe repository and can be obtained at http://hdl.handle.net/21.11116/0000-0007-7887-A. Model output used for the analysis is archived in the DRKZ long term archive LTA DOKU and can be obtained (http://cera-www.dkrz.de/WDCC/ui/Compact.jsp?acronym=DKRZ_LTA_033_ds00009, Specht et al., 2021).

References

Bourlès, B., Araujo, M., McPhaden, M. J., Brandt, P., Foltz, G. R., Lumpkin, R., et al. (2019). PIRATA: A sustained observing system for tropical Atlantic climate research and forecasting. *Earth and Space Science*, *6*(4), 577–616. https://doi.org/10.1029/2018ea000428

Brandt, P., Claus, M., Greatbatch, R. J., Kopte, R., Toole, J. M., Johns, W. E., & Böning, C. W. (2016). Annual and semiannual cycle of equatorial Atlantic circulation associated with basin-mode resonance. *Journal of Physical Oceanography*, *46*(10), 3011–3029. https://doi.org/10.1175/jpo-d-15-0248.1

Brandt, P., Hormann, V., Körtzinger, A., Visbeck, M., Krahmann, G., Stramma, L., & Schmid, C. (2010). Changes in the ventilation of the oxygen minimum zone of the tropical North Atlantic. *Journal of Physical Oceanography*, *40*(8), 1784–1801. https://doi.org/10.1175/2010jpo4301.1

Bunge, L., Provost, C., & Kartavtseff, A. (2007). Variability in horizontal current velocities in the central and eastern equatorial Atlantic in 2002. *Journal of Geophysical Research*, *112*(C2), C02014. https://doi.org/10.1029/2006jc003704

Busalacchi, A. J., & Picaut, J. (1983). Seasonal variability from a model of the tropical Atlantic Ocean. *Journal of Physical Oceanography*, *13*(9), 1564–1588. https://doi.org/10.1175/1520-0485(1983)013<1564:svfamo>2.0.co;2

Cabos, W., de la Vara, A., & Koseki, S. (2019). Tropical Atlantic variability: Observations and modeling. *Atmosphere*, *10*(9), 502. https://doi.org/10.3390/atmos10090502

Carton, J. A., Cao, X., Giese, B. S., & Da Silva, A. M. (1996). Decadal and interannual SST variability in the tropical Atlantic Ocean. *Journal of Physical Oceanography*, *26*(7), 1165–1175. https://doi.org/10.1175/1520-0485(1996)026<1165:daisvi>2.0.co;2

Cummins, P. F., Masson, D., & Saenko, O. A. (2016). Vertical heat flux in the ocean: Estimates from observations and from a coupled general circulation model. *Journal of Geophysical Research: Oceans*, *121*(6), 3790–3802. https://doi.org/10.1002/2016jc011647

de Decco, H. T., Junior, A. R. T., Pezzi, L. P., & Landau, L. (2018). Revisiting tropical instability wave variability in the Atlantic ocean using SODA reanalysis. *Ocean Dynamics*, *68*(3), 327–345. https://doi.org/10.1007/s10236-017-1128-2

Deppenmeier, A.-L., Haarsma, R. J., & Hazeleger, W. (2016). The Bjerknes feedback in the tropical Atlantic in CMIP5 models. *Climate Dynamics*, *47*(7–8), 2691–2707. https://doi.org/10.1007/s00382-016-2992-z

Foltz, G. R., Hummels, R., Dengler, M., Perez, R. C., & Araujo, M. (2020). Vertical turbulent cooling of the mixed layer in the Atlantic ITCZ and trade wind regions. *Journal of Geophysical Research: Oceans*, *125*, e2019JC015529. https://doi.org/10.1029/2019jc015529

Gaspar, P., Grégoris, Y., & Lefevre, J.-M. (1990). A simple eddy kinetic energy model for simulations of the oceanic vertical mixing: Tests at station papa and long-term upper ocean study site. *Journal of Geophysical Research*, *95*(C9), 16179–16193. https://doi.org/10.1029/jc095ic09p16179

Giorgetta, M. A., Brokopf, R., Crueger, T., Esch, M., Fiedler, S., Helmert, J., et al. (2018). Icon-a, the atmosphere component of the icon earth system model: I. model description. *Journal of Advances in Modeling Earth Systems*, *10*(7), 1613–1637. https://doi.org/10.1029/2017ms001242

Grodsky, S. A., Carton, J. A., Provost, C., Servain, J., Lorenzzetti, J. A., & McPhaden, M. J. (2005). Tropical instability waves at 0°N, 23°W in the Atlantic: A case study using Pilot research Moored Array in the Tropical Atlantic (PIRATA) mooring data. *Journal of Geophysical Research: Oceans*, *110*(C8), C08010. https://doi.org/10.1029/2005jc002941

Hersbach, H., Bell, B., Berrisford, P., Hirahara, S., Horányi, A., & Muñoz-Sabater, J., et al. (2020). The ERA5 global reanalysis. *Quarterly Journal of the Royal Meteorological Society*, *146*, 1999–2049.

Hersbach, H., Bell, B., Berrisford, P., Horányi, A., Sabater, J. M., Nicolas, J., et al. (2019). Global reanalysis: Goodbye ERA-interim, hello ERA5. *ECMWF newsletter*, *159*, 17–24.

Hormann, V., & Brandt, P. (2007). Atlantic equatorial undercurrent and associated cold tongue variability. *Journal of Geophysical Research*, *112*(C6), C06017. https://doi.org/10.1029/2006jc003931

Jochum, M., Malanotte-Rizzoli, P., & Busalacchi, A. (2004). Tropical instability waves in the Atlantic Ocean. *Ocean Modelling*, *7*(1–2), 145–163. https://doi.org/10.1016/s1463-5003(03)00042-8

Jochum, M., & Murtugudde, R. (2006). Temperature advection by tropical instability waves. *Journal of Physical Oceanography*, *36*(4), 592–605. https://doi.org/10.1175/jpo2870.1

Kalnay, E., Kanamitsu, M., Kistler, R., Collins, W., Deaven, D., Gandin, L., et al. (1996). The NCEP/NCAR 40-year reanalysis project. *Bulletin of the American Meteorological Society*, *77*(3), 437–472. https://doi.org/10.1175/1520-0477(1996)077<0437:tnyrp>2.0.co;2

Korn, P. (2017). Formulation of an unstructured grid model for global ocean dynamics. *Journal of Computational Physics*, *339*, 525–552. https://doi.org/10.1016/j.jcp.2017.03.009

Liu, C., Fang, L., Köhl, A., Liu, Z., Smyth, W. D., & Wang, F. (2019). The subsurface mode tropical instability waves in the equatorial Pacific Ocean and their impacts on shear and mixing. *Geophysical Research Letters*, *46*, 12270–12278. https://doi.org/10.1029/2019gl085123

Liu, C., Wang, X., Liu, Z., Köhl, A., Smyth, W. D., & Wang, F. (2020). On the formation of a subsurface weakly sheared laminar layer and an upper thermocline strongly sheared turbulent layer in the eastern Equatorial Pacific: Interplays of multiple-time-scale equatorial waves. *Journal of Physical Oceanography*, *50*(10), 2907–2930. https://doi.org/10.1175/jpo-d-19-0245.1

Lübbecke, J. F., Rodríguez-Fonseca, B., Richter, I., Martín-Rey, M., Losada, T., Polo, I., & Keenlyside, N. S. (2018). Equatorial Atlantic variability—Modes, mechanisms, and global teleconnections. *Wiley Interdisciplinary Reviews: Climate Change*, *9*(4), e527. https://doi.org/10.1002/wcc.527

Lumpkin, R., & Johnson, G. C. (2013). Global ocean surface velocities from drifters: Mean, variance, El Niño–Southern Oscillation response, and seasonal cycle. *Journal of Geophysical Research: Oceans*, *118*(6), 2992–3006. https://doi.org/10.1002/jgrc.20210

Masina, S., Philander, S., & Bush, A. (1999). An analysis of tropical instability waves in a numerical model of the Pacific Ocean: 2. Generation and energetics of the waves. *Journal of Geophysical Research*, *104*(C12), 29637–29661. https://doi.org/10.1029/1999jc900226

Muñoz, E., Weijer, W., Grodsky, S. A., Bates, S. C., & Wainer, I. (2012). Mean and variability of the tropical Atlantic Ocean in the CCSM4. *Journal of Climate*, *25*(14), 4860–4882. https://doi.org/10.1175/jcli-d-11-00294.1

Murtugudde, R. G., Ballabrera-Poy, J., Beauchamp, J., & Busalacchi, A. J. (2001). Relationship between zonal and meridional modes in the tropical Atlantic. *Geophysical Research Letters*, *28*(23), 4463–4466. https://doi.org/10.1029/2001gl013407

Perez, R. C., Foltz, G. R., Lumpkin, R., & Schmid, C. (2019). Direct measurements of upper ocean horizontal velocity and vertical shear in the tropical North Atlantic at 4°N, 23°W. *Journal of Geophysical Research: Oceans*, *124*(6), 4133–4151. https://doi.org/10.1029/2019jc015064

Prodhomme, C., Voldoire, A., Exarchou, E., Deppenmeier, A.-L., García-Serrano, J., & Guemas, V. (2019). How does the seasonal cycle control equatorial Atlantic interannual variability? *Geophysical Research Letters*, *46*(2), 916–922. https://doi.org/10.1029/2018gl080837

Proehl, J. A. (1996). Linear stability of equatorial zonal flows. *Journal of Physical Oceanography*, *26*(4), 601–621. https://doi.org/10.1175/1520-0485(1996)026<0601:lsoezf>2.0.co;2

Röske, F. (2006). A global heat and freshwater forcing dataset for ocean models. *Ocean Modelling*, *11*(3–4), 235–297. https://doi.org/10.1016/j.ocemod.2004.12.005

Specht, M. S., Jungclaus, J., & Bader, J. (2021). *Characterizing subsurface tropical instability waves in the Atlantic Ocean in simulations and observations*. World Data Center for Climate (WDCC) at DKRZ. Retrieved from http://cera-www.dkrz.de/WDCC/ui/Compact.jsp?acronym=DKRZ_LTA_033_ds00009

Steele, M., Morley, R., & Ermold, W. (2001). PHC: A global ocean hydrography with a high-quality Arctic Ocean. *Journal of Climate*, *14*(9), 2079–2087. https://doi.org/10.1175/1520-0442(2001)014<2079:pagohw>2.0.co;2

Storch, J.-S. V., Eden, C., Fast, I., Haak, H., Hernández-Deckers, D., Maier-Reimer, E., & Stammer, D. (2012). An estimate of the Lorenz energy cycle for the world ocean based on the STORM/NCEP simulation. *Journal of Physical Oceanography*, *42*(12), 2185–2205. https://doi.org/10.1175/jpo-d-12-079.1

Tourre, Y. M., Rajagopalan, B., & Kushnir, Y. (1999). Dominant patterns of climate variability in the Atlantic Ocean during the last 136 years. *Journal of Climate*, *12*(8), 2285–2299. https://doi.org/10.1175/1520-0442(1999)012<2285:dpocvi>2.0.co;2

von Schuckmann, K., Brandt, P., & Eden, C. (2008). Generation of tropical instability waves in the Atlantic Ocean. *Journal of Geophysical Research*, *113*(C8), C08034. https://doi.org/10.1029/2007jc004712

Wang, M., Xie, S.-P., Shen, S. S., & Du, Y. (2020). Rossby and yanai modes of tropical instability waves in the equatorial Pacific ocean and a diagnostic model for surface currents. *Journal of Physical Oceanography*, *50*(10), 3009–3024. https://doi.org/10.1175/jpo-d-20-0063.1

Xie, S.-P., & Carton, J. A. (2004). Tropical Atlantic variability: Patterns, mechanisms, and impacts. *Earth climate: The ocean-atmosphere interaction*. *Geophysical Monograph Series*, *147*, 121–142.

Zängl, G., Reinert, D., Rípodas, P., & Baldauf, M. (2015). The ICON (ICOsahedral Non-hydrostatic) modelling framework of DWD and MPI-M: Description of the non-hydrostatic dynamical core. *Quarterly Journal of the Royal Meteorological Society*, *141*(687), 563–579. https://doi.org/10.1002/qj.2378